Instability and propagation of EMIC waves in the magnetosphere by a kappa distribution

Qinghua Zhou,[1,2] Fuliang Xiao,[1,2] Jiankui Shi,[2] and Lijun Tang[1]

Received 25 October 2011; revised 4 March 2012; accepted 16 April 2012; published 1 June 2012.

[1] Electromagnetic ion cyclotron (EMIC) waves are excited near the magnetic equator by anisotropic ring current ions with energies near a few tens of keV. We investigate the instability and the path-integrated gain of EMIC waves during wave propagation. Calculations are performed by a global core density model, a field-aligned density model and particularly the hot ring current ions modeled by a kappa distribution. Simulating results show that the instability of EMIC waves is influenced primarily by the parameters of hot ring current ions, the wave normal angle and the composition of background plasma. A larger path-integrated gain occurs when the initial wave vector points toward lower L shells. During the storm main phase, the most common EMIC wave is the He^+ band wave which occurs in the outer magnetosphere beyond the plasmapause with frequency just below the cyclotron frequency of He^+. During the recovery phase, EMIC wave occurs in H^+ band and He^+ band with almost the same intensity in cases of interest. The O^+ band EMIC waves are very weak and quite rare. This result presents a further insight into propagation and instability of EMIC waves under different geomagnetic activities.

Citation: Zhou, Q., F. Xiao, J. Shi, and L. Tang (2012), Instability and propagation of EMIC waves in the magnetosphere by a kappa distribution, *J. Geophys. Res.*, *117*, A06203, doi:10.1029/2011JA017296.

1. Introduction

[2] Electromagnetic ion cyclotron EMIC waves, classified as Pc1-2 waves (0.1–5.0 Hz), are excited as left-hand polarized waves through wave-particle interaction. It is generally accepted that the energy for EMIC wave growth is provided by anisotropic ring current ions, with energies near a few tens of keV [*Mauk and McPherron*, 1980; *Roux et al.*, 1982]. Previous works [*Cornwall*, 1965; *Loto'aniu et al.*, 2005] indicate that the equatorial region is favored for EMIC wave generation. EMIC waves basically propagate along geomagnetic field lines. As the wave propagates to higher latitudes, the wave normal becomes highly inclined to the ambient magnetic field and wave energy can be absorbed by cyclotron resonant interaction with ambient ions [*Thorne and Horne*, 1994]. EMIC waves can also be guided by density gradients at the plasmapause, which keeps the wave normal angle small and significantly enhances the path integrated gain [*Thorne and Horne*, 1997].

[3] EMIC waves can occur in three distinct bands below the gyrofrequencies of H^+, He^+ and O^+. Here we define the H^+ band with frequencies $f_{He+} < f < f_{H+}$, the He^+ band, $f_{O+} < f < f_{He+}$ and the O^+ band $f < f_{O+}$. The frequencies f_{He+}, f_{H+} and f_{O+} are the gyrofrequencies of helium, hydrogen and oxygen respectively. Previous observational work has demonstrated that He^+ band occurs most commonly, with much higher wave intensity than H^+ and O^+ bands [*Fraser et al.*, 2010]. The majority of the EMIC wave events are observed in the afternoon sector, between 1300 and 2000 MLT [*Fraser and Nguyen*, 2001; *Meredith et al.*, 2003]. In this sector the EMIC occurrence rate increases with the radial distance (L shell) in the region $3 < L < 9$. Based on the observation of IMAGE-EUV, *Fraser et al.* [2005] have first associated EMIC waves with the drainage plumes. Recent study [*Chen et al.*, 2009] has shown that the drainage plume is highly structured. This density structure can support wave guiding and enhance the wave excitation within the plume, especially at frequencies close to the He^+ gyrofrequency.

[4] While EMIC waves may be observed during nonstorm periods, they are found to be most common and most intense during geomagnetic storms. The EMIC wave occurrence rate can be enhanced by a factor of five during the main and recovery storm phases, compared with nonstorm quieter times [*Erlandson and Ukhorskiy*, 2001]. Recently, *Fraser et al.* [2010] have investigated the association of EMIC waves with the various storm phases by checking 22 storms, and found that EMIC occurred during the main phases of 13 storms. *Halford et al.* [2010] have reported that 56.25% of storm time EMIC waves occur during the main phase, while 35.57% are observed in the recovery phase.

[5] In recent years EMIC wave has attracted considerable research interest because it plays an important role in ring current ion losses and radiation belt electron losses during geomagnetic storms via wave-particle interaction [*Fok et al.*,

[1]School of Physics and Electronic Sciences, Changsha University of Science and Technology, Changsha, China.
[2]State Key Laboratory of Space Weather, Chinese Academy of Sciences, Beijing, China.

Corresponding author: Q. Zhou, School of Physics and Electronic Sciences, Changsha University of Science and Technology, Changsha, 410004, China. (tedchow@163.com)

0148-0227/12/2011JA017296

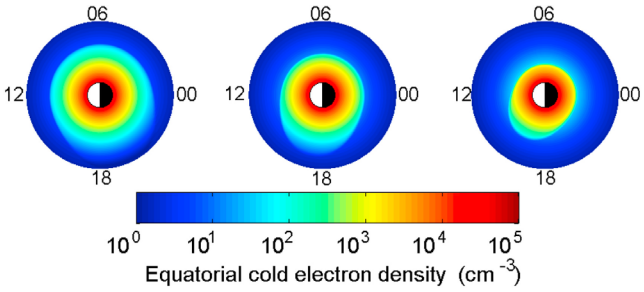

Figure 1. The equatorial background electron density for geomagnetic activity index. (left) K_p = 2, (middle) 4, and (right) 6.

1996; *Jordanova et al.*, 2001, 2008]. Previous works have investigated the excitation, propagation properties, energy transfer and the global distribution of EMIC waves by the HOTRAY code [*Horne and Thorne*, 1993, 1994]. However, their calculations focus on the cases where the energetic ion distribution follows the Ashour-Abdalla and Kennel distribution. During storm conditions, the injected energetic ions basically exhibit a pronounced non-Maxwellian high-energy tail distribution [*Lui and Krimigis*, 1981; *Viñas et al.*, 2005]. Such a distribution can be well modeled by a generalized Lorentzian (kappa) distribution [*Vasyliunas*, 1968; *Christon et al.*, 1988; *Xiao et al.*, 2008a]. *Summers and Thorne* [1991, 1992] have introduced the modified plasma dispersion function based on a kappa distribution function. *Xue et al.* [1996a, 1996b] have investigated the growth and damping of EMIC waves by a kappa distribution. Their results show that for small wave normal angles the Maxwellian distribution tends to overestimate the maximum wave growth rate, while for large wave normal angles the differences in growth rate between kappa distribution and Maxwellian distribution are small. *Xiao et al.* [2007a] have discussed the instability threshold condition of hot protons by kappa distribution for the EMIC waves. However, as far as we are aware, a systematic study on instability and propagation of EMIC waves in the magnetosphere by a kappa distribution has seldom been reported so far.

[6] In this study, ray tracing calculations are performed by incorporation of a global core plasma density model [*Gallagher et al.*, 2000] and a field-aligned density model for the background particle population [*Denton et al.*, 2002]. The formulation of [*Kennel*, 1966] base on a kappa distribution function is solved to evaluate the growth rate of EMIC waves and analyze the influence factors on growth rate. The results of ray trace are applied in the calculation of local growth rate. The path-integrated gain of EMIC waves is obtained by integrating local growth rate along the raypath.

2. Ray Tracing Model

[7] We adopt a recently developed program [*Zhou et al.*, 2010; *Xiao et al.*, 2007b, 2008b] which is based on the methodology of the HOTRAY code [*Horne*, 1989]. This program determines the raypath and the wave normal angle by integrating Hamilton's equations [*Horne*, 1989; *Suchy*, 1981]. The ray tracing method assumes that the plasma density gradient and the magnetic field gradient are small compared to the wavelength, and that the gradients remain continuous. The code checks the validity of Wentzel-Kramers- Brillouin (WKB) approximation at every step along the raypath.

[8] We adopt a dipole magnetic field model and a plasma density model which combines the global core plasma model [*Carpenter and Anderson*, 1992; *Gallagher et al.*, 1995, 2000] and the field-aligned density variation model [*Denton et al.*, 2002]:

$$N_c = N_{ce}(L/R)^{\alpha} \tag{1}$$

$$\alpha = 1.66 + 0.565x - 0.465x^2 + 0.0630x^3 \tag{2}$$

$$x = 8 - L \tag{3}$$

where N_c is the cold electron density, R is the radial distance from the center of the Earth in unit of the earth radius, L denotes the maximum radial distance of a magnetic field line in unit of the earth radius, N_{ce} is the density at the equatorial point along the field line passing the specific point associated with the global core density model.

[9] The global core plasma density model incorporates the plasmasphere and plasmapause density and the trough density, and considers the effect of Kp index and MLT on the density distribution [*Carpenter and Anderson*, 1992; *Gallagher et al.*, 1995, 2000]. The equatorial background electron density for different geomagnetic activity conditions is illustrated in Figure 1. The plasmapause extents to higher altitudes at afternoon to evening MLT to form a blunt bulge. As K_p increases the plasmapause moves inward closer to the Earth and the bulge region rotates sunward (westward).

3. Numerical Results

3.1. Local Growth Rate of EMIC Wave

[10] We calculate the local growth rate of EMIC waves following the previous works [*Kennel*, 1966; *Chen et al.*, 2010].

$$\begin{aligned}\gamma_s = {} & 2\pi^2 \frac{\omega_{ps}^2}{\omega|k_\parallel|\frac{\partial D^{(0)}}{\partial\omega}} \int_0^{\infty} v_\perp dv_\perp \int_{-\infty}^{+\infty} dv_\parallel \sum_m \delta\left(v_\parallel - \frac{\omega - m\Omega_s}{k_\parallel}\right) \\ & \cdot \left[G_{1s}\left((P - n^2\sin^2\psi)\left[2(L - n^2)v_\perp J_{m+1}^2 + 2v_\perp(R - n^2)J_{m-1}^2\right.\right.\right. \\ & + n^2\sin^2\psi v_\perp(J_{m+1} - J_{m-1})^2\left.\right] \\ & - n^2\cos\psi\,\sin\psi\left[2v_\parallel J_m\left(J_{m+1}(R - n^2) + J_{m-1}(L - n^2)\right)\right. \\ & \left.\left. + n^2\cos\psi\,\sin\psi v_\perp(J_{m+1} - J_{m-1})^2\right]\right) \\ & + G_{2s}\left(4v_\parallel J_m\left[(L - n^2)(R - n^2) + n^2\sin^2\psi(S - n^2)\right]\right. \\ & \left. - 2n^2\cos\psi\sin\psi\left[(R - n^2)v_\perp J_{m-1} + (L - n^2)v_\perp J_{m+1}\right]\right)\Big]\end{aligned} \tag{4}$$

where s denotes hot species and the subscript, γ_s is the local growth rate due to the contribution of hot species s, R, L, P and S are Stix notations of the cold plasma wave, n is the wave refractive index, ω is the wave frequency, ψ is the wave normal angle between wave vector and filed line, $\psi > 0$ or $\psi < 0$ occurs when wave vector points toward higher L shell or lower L shell in our calculation, respectively. m denotes the harmonic resonance, J_m are Bessel functions of order m.

We set the range of m from -10 to 10 in our calculation. $D^{(0)}$ is the determinant of the cold plasma wave dispersion relation matrix defined as

$$D^{(0)} = \begin{vmatrix} 2\left(R - n^2 + \frac{1}{2}n^2\sin^2\psi\right) & n^2\sin^2\psi & n^2\cos\psi\sin\psi \\ n^2\sin^2\psi & 2\left(L - n^2 + \frac{1}{2}n^2\sin^2\psi\right) & n^2\cos\psi\sin\psi \\ n^2\cos\psi\sin\psi & n^2\cos\psi\sin\psi & P - n^2\sin^2\psi \end{vmatrix} \quad (5)$$

G_1 and G_2 are defined as

$$G_{1s} = \frac{\partial F_s}{\partial v_\perp} - \frac{k_\parallel}{\omega}\left(v_\parallel\frac{\partial F_s}{\partial v_\perp} - v_\perp\frac{\partial F_s}{\partial v_\parallel}\right) \quad (6)$$

and

$$G_{2s} = J_m\left[\frac{\partial F_s}{\partial v_\parallel} + \frac{m\Omega_s}{\omega v_\perp}\left(v_\parallel\frac{\partial F_s}{\partial v_\perp} - v_\perp\frac{\partial F_s}{\partial v_\parallel}\right)\right] \quad (7)$$

where F_s is the normalized distribution function of hot species s.

[11] We assume the equatorial distribution function for hot ion species s as a kappa distribution:

$$F_s\left(v_{\parallel e}, v_{\perp e}\right) = \frac{N_{hes}\Gamma(\kappa+1)}{\pi^{3/2}\theta_{\perp e}^2\theta_{\parallel e}\kappa^{3/2}\Gamma(\kappa-1/2)}\left[1 + \frac{v_{\parallel e}^2}{\kappa\theta_{\parallel e}^2} + \frac{v_{\perp e}^2}{\kappa\theta_{\perp e}^2}\right]^{-(\kappa+1)} \quad (8)$$

with associated parallel and perpendicular effective thermal speeds at the equator

$$\theta_{\parallel e} = \left(\frac{2\kappa-3}{\kappa}\right)^{1/2}\left(\frac{T_{\parallel e}}{m_s}\right)^{1/2} \quad (9)$$

$$\theta_{\perp e} = \left(\frac{2\kappa-3}{\kappa}\right)^{1/2}\left(\frac{T_{\perp e}}{m_s}\right)^{1/2} \quad (10)$$

where Γ is the gamma function, m_s is the rest mass of species s, $T_{\parallel e}$ and $T_{\perp e}$ are temperatures parallel and perpendicular to the ambient magnetic field respectively at the equator. The temperature anisotropy of hot species s at the equator is

$$A_e = \frac{T_{\perp e}}{T_{\parallel e}} - 1 \quad (11)$$

When energetic ions move along the Earth's magnetic field line, the anisotropy and number density vary with the latitude due to the conservation of the first adiabatic invariant and total electron energy. Currently, there is lack of direct observational information about distribution of energetic ions along the magnetic latitude. We adopt a field-aligned density model for hot species s [*Xiao and Feng*, 2006].

$$F_s\left(v_\parallel, v_\perp\right) = \frac{N_{hs}\Gamma(\kappa+1)}{\pi^{3/2}\theta_\perp^2\theta_\parallel\kappa^{3/2}\Gamma(\kappa-1/2)}\left[1 + \frac{v_\parallel^2}{\kappa\theta_\parallel^2} + \frac{v_\perp^2}{\kappa\theta_\perp^2}\right]^{-(\kappa+1)} \quad (12)$$

with effective thermal speeds and temperatures parallel and perpendicular to the ambient magnetic field at the magnetic latitude λ as follows:

$$\theta_\parallel^2(\lambda) = \theta_{\parallel e}^2 \quad (13)$$

$$\theta_\perp^2(\lambda) = \theta_{\perp e}^2\left[(A_e+1) - A_e\frac{\cos^6\lambda}{\left(1+3\sin^2\lambda\right)^{1/2}}\right]^{(-1)} \quad (14)$$

where N_{hs} is the density of hot species s.

[12] Numerical solutions to equation (4) are obtained in Figures 1–5 by adopting the typical storm time value of ion composition of cold plasma: η_{H^+} = 77%, η_{He^+} = 20% and η_{O^+} = 3% [*Jordanova et al.*, 2008], and a Sunspot number = 100, representative of a relatively high solar activity [*Carpenter and Anderson*, 1992]. Figure 2 shows the influence of anisotropy, temperature and density of energetic protons on the local growth rate of EMIC wave. Simulations are performed with parameters K_p = 6, L = 6, MLT = 14, λ = 0, ψ = 0 and κ = 2. The growth rate of EMIC wave increases with three factors above in all three bands. The Figure 2 (top) shows the influence of anisotropy of energetic protons on the local growth rate. H^+ band instability occurs only when $A_e \geq 1.2$ at $T_{\parallel e}$ = 50 keV and N_{H^+} = 2 cm^{-3}. The Figure 2 (middle) shows the influence of temperature of energetic protons on the local growth rate, with fixed anisotropy A_e = 1.5 and density N_{H^+} = 2 cm^{-3}. The local growth rate increases with increasing energy under the fixed temperature and density. The Figure 2 (bottom) shows the influence of density of energetic protons on the local growth rate. If the density of hot proton is relatively low (e.g., 0.2 cm^{-3}), the instability is very weak even when the anisotropy or temperature is high (e.g., A_e = 1.5 and $T_{\parallel e}$ = 50 keV). Consequently, the suprathermal protons with a high density and a high temperature anisotropy are essential to the excitation of EMIC wave.

[13] The local growth rates of EMIC waves at different equatorial locations ($3 \leq L \leq 6$) are shown in Figure 3 (top). The growth rate increases with L increasing, consistent with observations [*Fraser and Nguyen*, 2001; *Meredith et al.*, 2003]. As shown in Figure 3 (middle), the growth rate decreases dramatically with increasing geomagnetic latitude, particularly in H^+ band. The growth rate at $\lambda > 15°$ is negligible, indicating that equatorial region is the favorable region for EMIC wave generation. This is supported by CRRES and other Poynting flux observations which show a source region within $\pm 11°$ of the equator [*Loto'aniu et al.*, 2005]. Figure 3 (bottom) shows the growth rate of EMIC waves for different wave normal angles. As the wave becomes more oblique there is a progressive decrease in wave growth rate due to either Landau damping or cyclotron resonant absorption. Wave damping occurs more significantly in He^+ band and O^+ band. For H^+ band waves, as the wave normal angle increases, wave growth rate decreases relatively slowly but the frequency range of EMIC instability becomes broader.

[14] The observations of ring current [*Fu et al.*, 2002; *Nosé et al.*, 2005] show that during magnetic storms, the abundance of hot O^+ increases dramatically and the growth of hot He^+ is not obvious. Previous studies show that hot O^+ (or

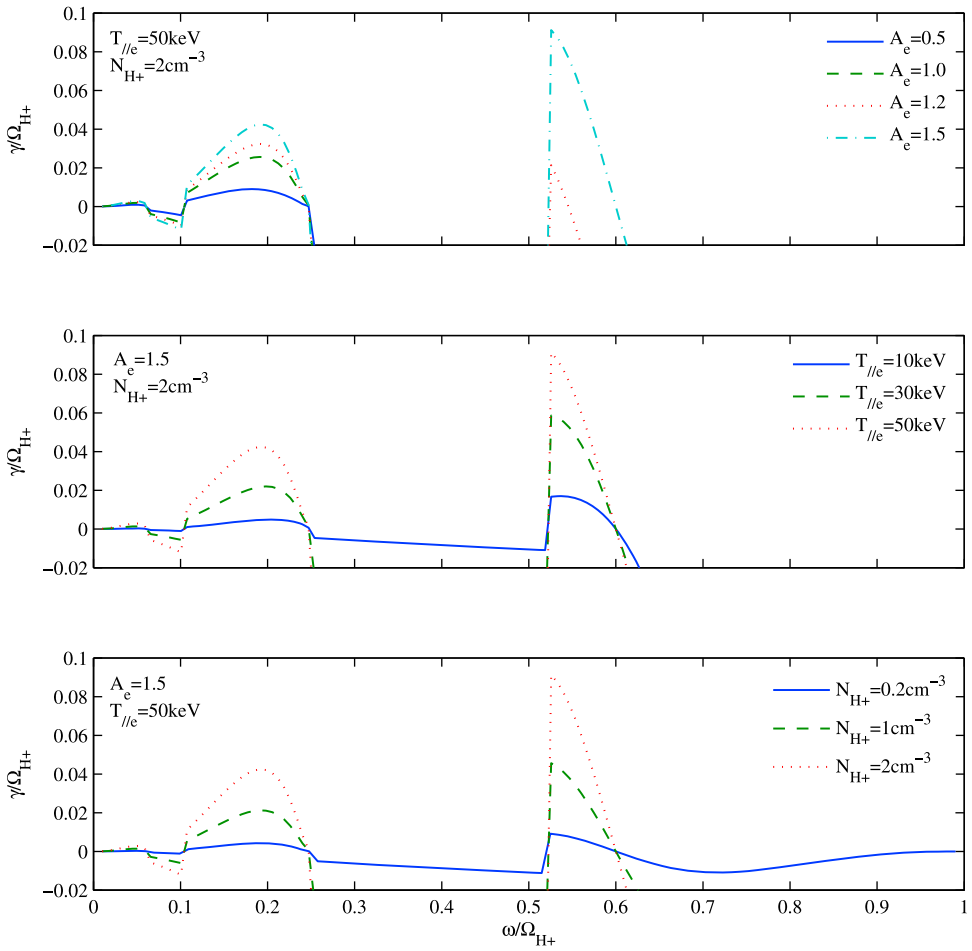

Figure 2. The influence of (top) anisotropy, (middle) temperature and (bottom) density of energetic protons on local growth rate.

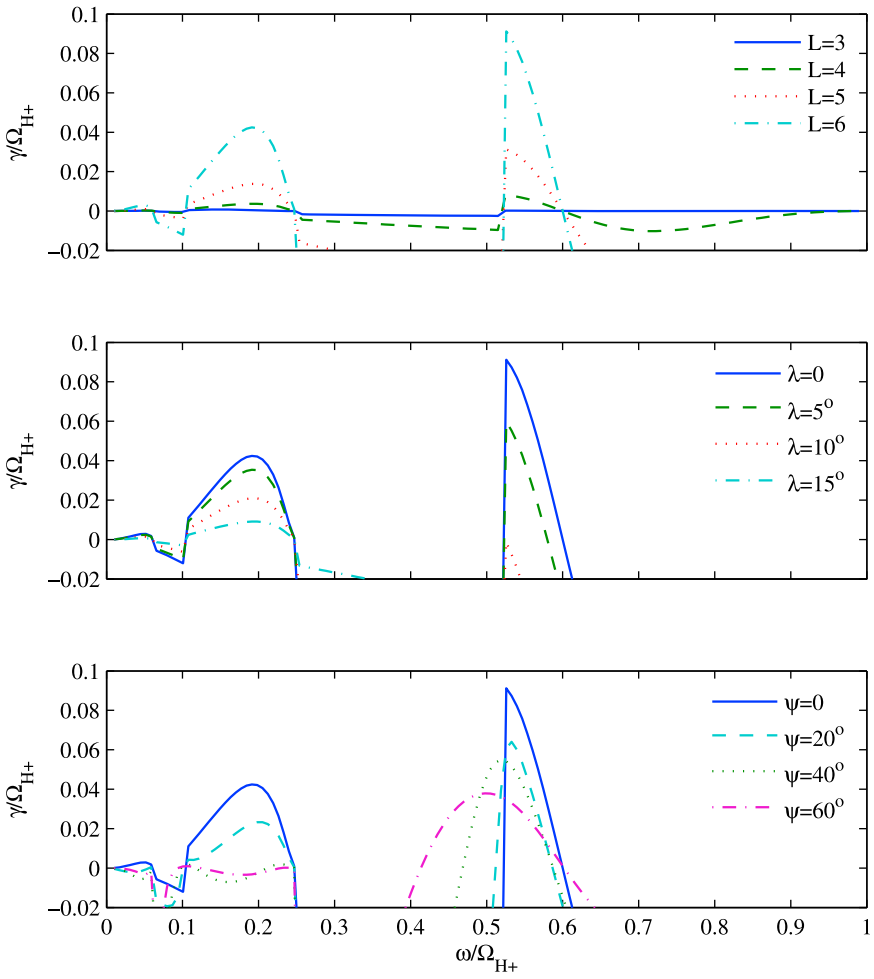

Figure 3. The local growth rates at (top) different equatorial locations, (middle) different latitude, and (bottom) for different wave normal angle.

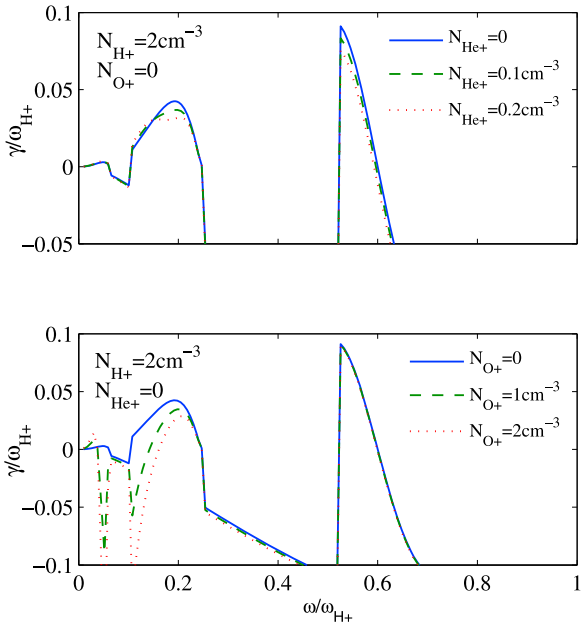

Figure 4. The influence of density of (top) hot He^+ and (bottom) hot O^+ on the local growth rate of EMIC wave.

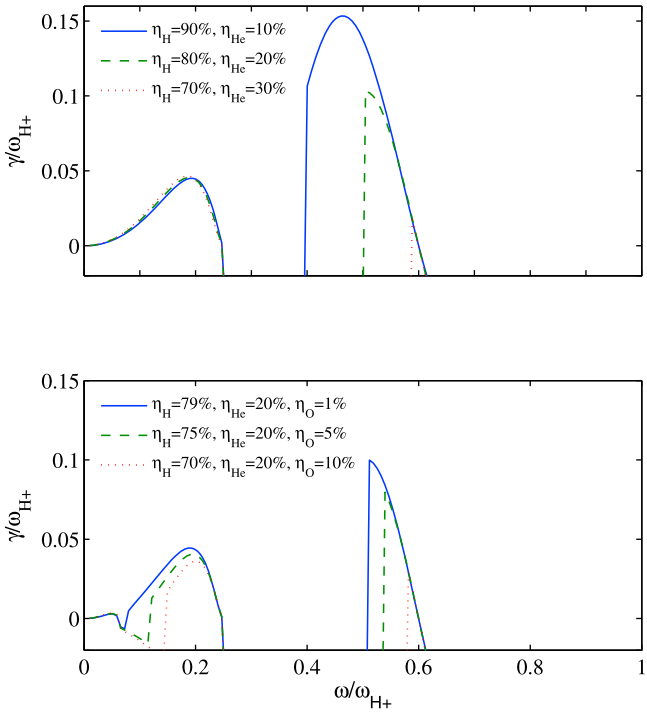

Figure 6. The influence of the ion fractional composition of cold plasma on growth rate: density variation of (top) He^+ ion and (bottom) O^+ ion.

He^+) ions suppress the growth rates at frequencies near the bi-ion frequency and harmonics gyrofrequency nf_{O+} (or nf_{He+}) by cyclotron resonant absorption [*Kozyra et al.*, 1984; *Thorne and Horne*, 1993]. Figure 4 shows the influence of hot He^+ (top) and hot O^+ (bottom) on the local growth rate of EMIC wave. We assume that the parallel temperatures at the equator of both hot He^+ and hot O^+ are 50 keV. Hot He^+ reduces the growth rate in both He^+ and H^+ bands but it has little effect in O^+ band. In contrast, hot O^+ has little effect in H^+ band, but reduces the growth rate in He^+ band. Furthermore, the growth rate in O^+ band increases with the increase in density of hot O^+ but remains relatively weak even when $N_{O+} = 2$ cm^{-3}, indicating that EMIC waves rarely occur in the band below the oxygen gyrofrequency.

[15] The growth rate of EMIC waves with different frequencies is presented in Figure 5, with parameters $A_e = 1.5$, $N_H = 2$ cm^{-3}, $N_{He+} = 0.1$ cm^{-3} and $N_{O+} = 0.5$ cm^{-3}. Obviously, He^+ band instability region is broadest, suggesting that the most common EMIC wave in the magnetosphere is He^+ band. In addition, the wave instability at lower frequency tends to occur in a larger L-shell region, with a larger growth rate, consistent with the observation that EMIC waves occur most common in the outer magnetosphere beyond the plasmapause.

[16] Since the typical composition of cold heavy ions He^+ and O^+ lies in the range from 10% to 20% and from 1% to 10%, respectively [*Farrugia et al.*, 1989; *Hu and Fraser*, 1994], We choose different composition of cold heavy ions to study the effect of the ion fractional composition on growth rate, as shown in Figure 6. The presence of He^+ ions

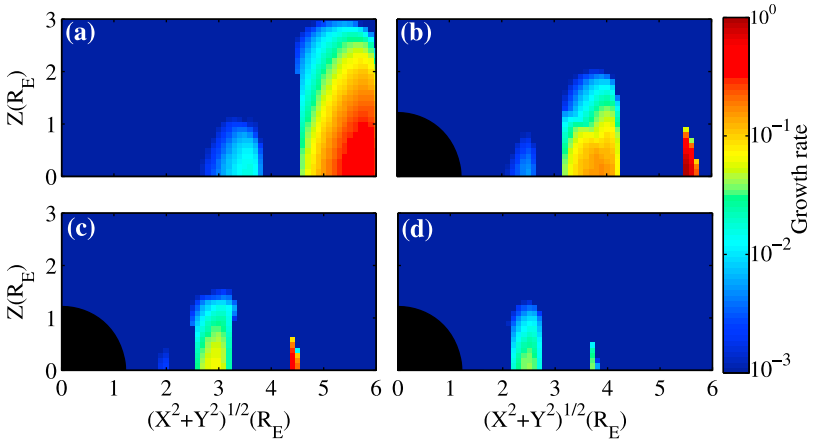

Figure 5. Local growth rate of EMIC waves with different frequencies: (a) 0.5 Hz, (b) 1.5 Hz,(c) 3.0 Hz and (d) 5.0 Hz in the meridian plane of MLT = 14 during $K_p = 6$. The center of bulge is located at $L = 4.0$.

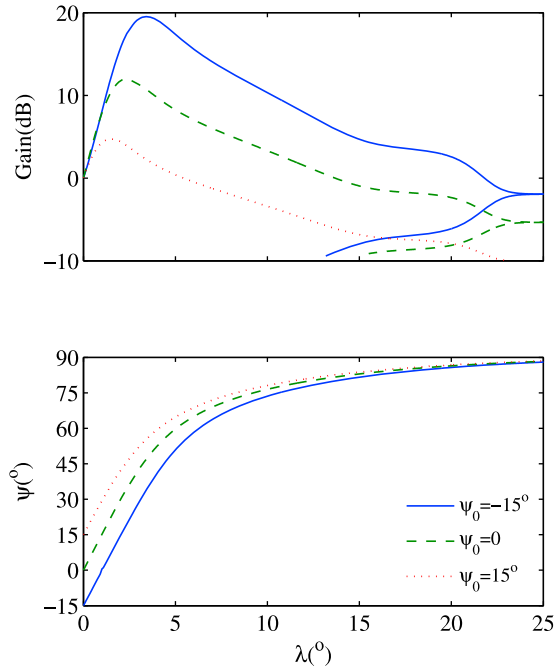

Figure 7. (a) Path-integrated gain and (b) the wave normal angle versus magnetic latitude. The waves launched at L = 6.0, with a fixed frequency 0.48 Hz ($\sim 0.22 f_{H+}$) but different initial wave angles: $\psi_0 = -15°$ (solid), 0 (dashed) and 15° (dotted).

significantly reduces the growth rate in H^+ band, but has little influence on He^+ band and O^+ band (see Figure 6, top). The increase in He^+ cold population reduces the emission bandwidth of H^+ band waves due to an increase in the L mode cutoff frequency [*Horne and Thorne*, 1994]. The H^+ band waves between the cutoff frequency and the crossover frequency propagate in the unguided mode [*Rauch and Roux*, 1982; *Horne and Thorne*, 1993]. Such unguided waves have very small wave gains. Strong instability of guided waves in the H^+ band occurs preferentially for a lower He^+ concentration [*Horne and Thorne*, 1994; *Xue et al.*, 1996b]. Similarly, the increase in O^+ cold population reduces the emission bandwidth of H^+ band and He^+ band waves and significantly reduces the growth rate in H^+ band and He^+ band (see Figure 6, bottom).

3.2. Path-Integrated Gain

[17] In the following, for a direct comparison we shall use the same storm-time value of ion composition of cold plasma as above: η_{H+} = 77%, η_{He+} = 20% and η_{O+} = 3%. The path-integrated wave gain in dB is calculated by integrating the local growth rate along the raypath:

$$Gain = 20 \log_{10}\left(\exp\left(\int \gamma dt\right)\right). \quad (15)$$

[18] Figure 7 shows the path-integrated gain and the wave normal angle as a function of the magnetic latitude λ for He^+ band EMIC waves launched at the equatorial location L = 6.0 for different initial wave normal angles. The path-integrated gain increases when the EMIC waves starts out from the equatorial plane. As the waves propagate toward higher latitudes their wave normal angles increase, allowing wave damping to dominate over the cyclotron growth. The wave gains maximize at λ = 3.4, 2.4 and 1.5 for $\psi_0 = -15°$, 0 and 15° respectively. A larger path-integrated gain occurs when the initial wave vector points toward the lower L shells ($\psi_0 = -15°$), probably because the wave propagates less obliquely than at cases ψ_0 = 0 and ψ_0 = 15°, and correspondingly the wave damping is less at $\psi_0 = -15°$. This also occurs in H^+ band and O^+ band EMIC waves. He^+ band waves suffer reflection where their frequency matches the local $O^+ - He^+$ bi-ion frequency. The reflected waves experience significant cyclotron resonant absorption near the reflection point, as discussed by *Perraut et al.* [1984] and *Thorne and Horne* [1993].

[19] In Figure 8, we illustrate the path-integrated gain of EMIC waves launched at equatorial L = 6.0 with frequencies near peak growth rate in He^+ band and H^+ band. All waves are initiated with ψ = 0. Waves with frequencies around $0.22 f_{H+}$ and $0.54 f_{H+}$ approach the maximum gain in He^+ band and H^+ band, respectively. He^+ band waves are reflected near the $H^+ - He^+$ bi-ion frequency.

[20] It should be noted that the calculations above are carried out only for one-side equatorial wave propagation. The maximum wave gain would be twice if waves are launched from one side and travel toward the other side of the equator [*Chen et al.*, 2010]. In Figures 9 and 10 we consider two-side equatorial wave propagations and show the maximum wave gain of EMIC waves with ψ = 0 at the equator as a function of L and frequency in the meridian plane of MLT = 14 during the storm main phase (K_p = 6) and

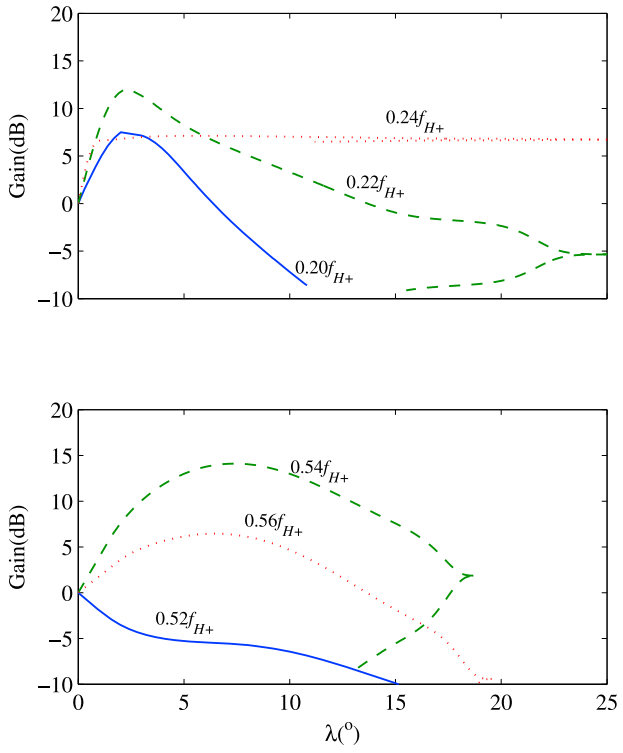

Figure 8. The path-integrated gain of EMIC waves with different frequencies in (top) He^+ band and (bottom) H^+ band.

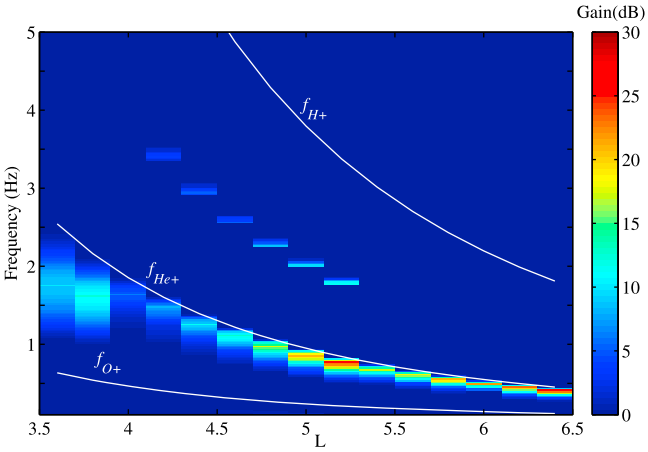

Figure 9. The path-integrated gain of EMIC waves as a function of L and frequency in the meridian plane of MLT = 14 during the storm main phase.

recovery phase ($K_p = 4$). The plasmapause locates at $L = 4.0$ when $K_p = 6$ and moves outward to $L = 4.6$ when $K_p = 4$. The typical values of hot ions parameters at each location are listed in Table 1 [*Fu et al.*, 2002; *Jordanova et al.*, 2006; *Chen et al.*, 2010].

[21] As shown in Figure 9, during the main phase the most common EMIC waves lie in He^+ band just below the cyclotron frequency of He^+ both inside and outside the plasmapause. In contrast, H^+ band wave exists mainly outside the plasmapause with a lower wave intensity and a relatively narrow frequency range. Furthermore, EMIC waves in O^+ band are very weak, below 5 dB.

[22] As shown in Figure 10, H^+ band EMIC waves are significantly enhanced both inside and outside the plasmapause since the temperature anisotropy increases during the storm recovery phase [*Chen et al.*, 2010]. This implies the H^+ band waves occur more preferably during recovery phase, consistent with previous statistical study [*Fraser et al.*, 2010]. However, the wave gains in He^+ band and O^+ band vary little during the recovery phase though the temperature

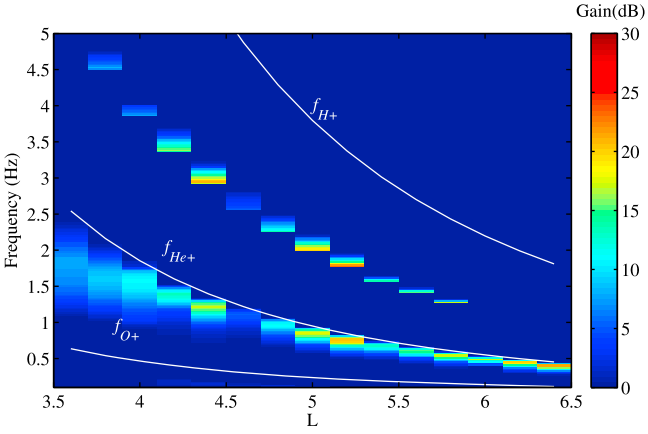

Figure 10. The path-integrated gain of EMIC waves as a function of L and frequency in the meridian plane of MLT = 14 during the storm recovery phase.

Table 1. The Parameters of Ring Current Energetic Ions[a]

L	N_{H+} (cm^{-3})	N_{He+} (cm^{-3})	(cm^{-3})	A_e
		Main Phase		
3.6∼4.0	2.0	0.1	0.8	1.1
4.2∼4.6	3.0	0.1	1.4	1.3
4.8∼5.2	3.5	0.1	1.7	1.3
5.4∼5.8	2.5	0.1	1.2	1.1
6.0∼6.4	2.0	0.1	0.8	1.1
		Recovery Phase		
3.6∼4.0	1.5	0.1	0.4	1.2
4.2∼4.6	2.2	0.1	0.7	1.5
4.8∼5.2	2.5	0.1	0.9	1.5
5.4∼5.8	2.0	0.1	0.6	1.2
6.0∼6.4	1.8	0.1	0.4	1.1

[a]For all the hot ions we assume $T_{\|e} = 50$ keV.

anisotropy increases. This is primarily because decreases in densities of ions reduce the growth rate at the same time.

4. Summary and Conclusion

[23] The EMIC waves can be excited in the magnetosphere by cyclotron resonant instability with anisotropic ring current ions. These ions basically exhibit a pronounced high-energy tail distribution which can be well modeled by a kappa distribution. Based on the kappa distribution model, the instability of EMIC waves and the path-integrated gain during propagation are discussed in detail. The major conclusions are obtained as follows.

[24] 1. In all three bands, the growth rate of EMIC wave increases as the anisotropy, the temperature or the density of energetic protons increases. A higher anisotropy is needed to excite the H^+ band waves than to excite the He^+ band waves.

[25] 2. The growth rate of EMIC waves increases monotonically with L shell in the region $3 \le L \le 6$ and decreases dramatically with geomagnetic latitude. As the wave normal angle increase, the wave is subject to either Landau damping or cyclotron resonant absorption, leading to a progressive decrease in wave growth rate.

[26] 3. As the density of hot He^+ increases, the growth rate in He^+ band and H^+ band is reduced, but the growth rate in O^+ band varies little. As the density of hot O^+ ions increases, the growth rate remains almost constant in H^+ band, reduces in He^+ band, and enhances in O^+ band.

[27] 4. As the density of cold He^+ increases, the growth rate in H^+ band is reduced significantly, but varies little in He^+ and O^+ bands. Meanwhile, increase in density of cold O^+ ions produces a substantial reduction in growth rate in H^+ and He^+ bands.

[28] 5. A larger path-integrated gain occurs when the initial wave vector points toward the lower L shells (e.g., $\psi_0 = -15°$), probably because the wave propagates less obliquely and correspondingly experiences less damping than the wave with initial wave vector parallel to the magnetic field or pointing toward higher L shells. During propagation to higher latitudes, highly oblique EMIC waves encounter reflection where the frequency matches the local bi-ion frequency and correspondingly suffer substantial cyclotron resonant absorption.

[29] 6. During the main phase, the He^+ band wave just below the cyclotron frequency of He^+ occurs most frequently

in the magnetosphere. During the recovery phase, H^+ band wave is enhanced with approximately the same intensity as that of He^+ band. However, the O^+ band waves are found to be very weak and quite rare.

[30] **Acknowledgments.** This work is supported by 973 Program 2012CB825603, the National Natural Science Foundation of China grants 40931053, 40925014, the Specialized Research Fund for State Key Laboratories, and the construct program of the key discipline in Hunan Province.

[31] Robert Lysak thanks the reviewers for their assistance in evaluating the paper.

References

Carpenter, D. L., and R. R. Anderson (1992), An ISEE/Whistler model of equatorial electron density in the magnetosphere, *J. Geophys. Res.*, *97*, 1097–1108.

Chen, L., R. M. Thorne, and R. B. Horne (2009), Simulation of EMIC wave excitation in a model magnetosphere including structured high-density plumes, *J. Geophys. Res.*, *114*, A07221, doi:10.1029/2009JA014204.

Chen, L., R. M. Thorne, V. K. Jordanova, C.-P. Wang, M. Gkioulidou, L. Lyons, and R. B. Horne (2010), Global simulation of emic wave excitation during the 21 April 2001 storm from coupled RCM-RAM-HOTRAY modeling, *J. Geophys. Res.*, *115*, A07209, doi:10.1029/2009JA015075.

Christon, S. P., D. G. Mitchell, D. J. Williams, L. A. Frank, C. Y. Huang, and T. E. Eastman (1988), Energy spectra of plasmasheet ions and electrons from 50 eV/e to 1 MeV during plasma temperature transitions, *J. Geophys. Res.*, *93*, 2562–2572.

Cornwall, J. M. (1965), Cyclotron instabilities and electromagnetic emission in the ultra low frequency and very low frequency ranges, *J. Geophys. Res.*, *70*, 61–69.

Denton, R. E., J. Goldstein, J. D. Menietti, and S. L. Young (2002), Magnetospheric electron density model inferred from Polar plasma wave data, *J. Geophys. Res.*, *107*(A11), 1386, doi:10.1029/2001JA009136.

Erlandson, R. E., and A. J. Ukhorskiy (2001), Observations of electromagnetic ion cyclotron waves during geomagnetic storms: Wave occurrence and pitch angle scattering, *J. Geophys. Res.*, *106*, 3883–3895.

Farrugia, C. J., J. G. D. T. Young, and H. Balsiger (1989), The composition, temperature, and density structure of cold ions in the quiet terrestrial plasmasphere: GEOS 1 results, *J. Geophys. Res.*, *94*, 11,865–11,891.

Fok, M.-C., T. E. Moore, and M. E. Greenspan (1996), Ring current development during storm main phase, *J. Geophys. Res.*, *101*, 15,311–15,322.

Fraser, B. J., and T. S. Nguyen (2001), Is the plasmapause a preferred source region of electromagnetic ion cyclotron waves in the magnetosphere?, *J. Atmos. Sol. Terr. Phys.*, *63*, 1225–1247.

Fraser, B. J., H. J. Singer, M. L. Adrian, D. L. Gallagher, and M. F. Thomsen (2005), The relationship between plasma density structure and EMIC waves at geosynchronous orbit, in *Inner Magnetosphere Interactions: New Perspectives From Imaging*, *Geophys. Monogr. Ser.*, vol. 159, pp. 55–70, AGU, Washington, D. C.

Fraser, B. J., R. S. Grew, S. K. Morley, J. C. Green, H. J. Singer, T. M. Loto'aniu, and M. F. Thomsen (2010), Storm time observations of electromagnetic ion cyclotron waves at geosynchronous orbit: GOES results, *J. Geophys. Res.*, *115*, A05208, doi:10.1029/2009JA014516.

Fu, S., Q. Zong, T. Fritz, Z. Pu, and B. Wilken (2002), Composition signature in ion injections and its dependence on geomagnetic conditions, *J. Geophys. Res.*, *107*(A10), 1299, doi:10.1029/2001JA002006.

Gallagher, D. L., P. D. Craven, R. H. Comfort, and T. E. Moore (1995), On the azimuthal variation of core plasma in the equatorial magnetosphere, *J. Geophys. Res.*, *100*, 23,597–23,605.

Gallagher, D. L., P. D. Craven, and R. H. Comfort (2000), Global core plasma model, *J. Geophys. Res.*, *105*, 18,819–18,833.

Halford, A. J., B. J. Fraser, and S. K. Morley (2010), EMIC wave activity during geomagnetic storm and nonstorm periods: CRRES results, *J. Geophys. Res.*, *115*, A12248, doi:10.1029/2010JA015716.

Horne, R. B. (1989), Path-integrated growth of electrostatic waves: The generation of terrestrial myriametric radiation, *J. Geophys. Res.*, *94*, 8895–8909.

Horne, R. B., and R. Thorne (1993), On the preferred source location for the convective amplification of ion cyclotron waves, *J. Geophys. Res.*, *98*, 9233–9247.

Horne, R. B., and R. Thorne (1994), Convective instabilities of electromagnetic ion cyclotron waves in the outer magnetosphere, *J. Geophys. Res.*, *99*, 17,259–17,273.

Hu, Y. D., and B. J. Fraser (1994), Electromagnetic ion cyclotron wave amplification and source regions in the magnetosphere, *J. Geophys. Res.*, *99*, 263–272.

Jordanova, V. K., C. J. Farrugia, R. M. Thorne, G. V. Khazanov, G. D. Reeves, and M. F. Thomsen (2001), Modeling ring current proton precipitation by electromagnetic ion cyclotron waves during the May 14–16, 1997, storm, *J. Geophys. Res.*, *106*, 7–22.

Jordanova, V. K., Y. S. Miyoshi, S. Zaharia, M. F. Thomsen, G. D. Reeves, D. S. Evans, C. G. Mouikis, and J. F. Fennell (2006), Kinetic simulations of ring current evolution during the geospace environment modeling challenge events, *J. Geophys. Res.*, *111*, A11S10, doi:10.1029/2006JA011644.

Jordanova, V. K., J. Albert, and Y. Miyoshi (2008), Relativistic electron precipitation by EMIC waves from self-consistent global simulations, *J. Geophys. Res.*, *113*, A00A10, doi:10.1029/2008JA013239.

Kennel, C. (1966), Low-frequency whistler mode, *Phys. Fluids*, *9*, 2190, doi:10.1063/1.1761588.

Kozyra, J. U., T. E. Cravens, A. F. Nagy, E. G. Fontheim, and R. S. B. Ong (1984), Effects of energetic heavy ions on electromagnetic ion cyclotron wave generation in the plasmapause region, *J. Geophys. Res.*, *89*, 2217–2233.

Loto'aniu, T. M., B. J. Fraser, and C. L. Waters (2005), Propagation of electromagnetic ion cyclotron wave energy in the magnetosphere, *J. Geophys. Res.*, *110*, A07214, doi:10.1029/2004JA010816.

Lui, A. T. Y., and S. M. Krimigis (1981), Earthward transport of energetic protons in the Earth's plasma sheet, *Geophys. Res. Lett.*, *8*, 527–530.

Mauk, B. H., and R. L. McPherron (1980), An experimental test of the electromagnetic ion cyclotron instability within the Earth's magnetosphere, *Phys. Fluids*, *23*, 2111, doi:10.1063/1.862873.

Meredith, N. P., R. M. Thorne, R. B. Horne, D. Summers, B. J. Fraser, and R. R. Anderson (2003), Statistical analysis of relativistic electron energies for cyclotron resonance with EMIC waves observed on CRRES, *J. Geophys. Res.*, *108*(A6), 1250, doi:10.1029/2002JA009700.

Nosé, M., S. Taguchi, K. Hosokawa, S. P. Christon, R. W. McEntire, T. E. Moore, and M. R. Collier (2005), Overwhelming O^+ contribution to the plasma sheet energy density during the October 2003 superstorm: Geotail/EPIC and IMAGE/LENA observations, *J. Geophys. Res.*, *110*, A09S24, doi:10.1029/2004JA010930.

Perraut, S., R. Gendrin, A. Roux, and C. de Villedary (1984), Ion cyclotron waves: Direct comparison between ground-based measurements and observations in the source region, *J. Geophys. Res.*, *89*, 195–202.

Rauch, J. L., and A. Roux (1982), Ray tracing of ulf waves in a multicomponent magnetospheric plasma: Consequences for the generation mechanism of ion cyclotron waves, *J. Geophys. Res.*, *87*, 8191–8198.

Roux, A., S. Perraut, J. Rauch, C. de Villedary, G. Kremser, A. Korth, and D. Young (1982), Wave-particle interactions near ω^+_{He} observed on board GEOS 1 and 2: 2. Generation of ion cyclotron waves and heating of He^+ ions, *J. Geophys. Res.*, *87*, 8174–8190, doi:10.1029/JA087iA10p08174.

Suchy, K. (1981), Real Hamilton equations of geomagnetic optics for media with moderate absorption, *Radio Sci.*, *16*, 1179–1182.

Summers, D., and R. M. Thorne (1991), The modified plasma dispersion function, *Phys. Fluids B*, *3*, 1835, doi:10.1063/1.859653.

Summers, D., and R. M. Thorne (1992), A new tool for analyzing microinstabilities in space plasmas modelled by a generalized Lorentzian (Kappa) distribution, *J. Geophys. Res.*, *97*, 16,827–16,832.

Thorne, R. M., and R. B. Horne (1993), Cyclotron absorption of ion-cyclotron waves at the bi-ion frequency, *Geophys. Res. Lett.*, *20*, 317–320, doi:10.1029/93GL00089.

Thorne, R. M., and R. B. Horne (1994), Energy transfer between energetic ring current H^+ and O^+ by electromagnetic ion cyclotron waves, *J. Geophys. Res.*, *99*, 17,275–17,282, doi:10.1029/94JA01007.

Thorne, R. M., and R. B. Horne (1997), Modulation of electromagnetic ion cyclotron instability due to interaction with ring current O^+ during magnetic storms, *J. Geophys. Res.*, *102*, 14,155–14,163.

Vasyliunas, V. M. (1968), A survey of low-energy electrons in the evening sector of the magnetosphere with OGO 1 and OGO 3, *J. Geophys. Res.*, *73*, 2839–2884.

Viñas, A. F., R. L. Mace, and R. F. Benson (2005), Dispersion characteristics for plasma resonances of Maxwellian and Kappa distribution plasmas and their comparisons to the IMAGE/RPI observations, *J. Geophys. Res.*, *110*, A06202, doi:10.1029/2004JA010967.

Xiao, F., and X. Feng (2006), Modeling density and anisotropy of energetic electrons along magnetic field lines, *Plasma Sci. Technol*, *8*, 279, doi:10.1088/1009-0630/8/3/07.

Xiao, F., Q. H. Zhou, H. Y. He, H. N. Zheng, and S. Wang (2007a), Electromagnetic ion cyclotron waves instability threshold condition of suprathermal protons by Kappa distribution, *J. Geophys. Res.*, *112*, A07219, doi:10.1029/2006JA012050.

Xiao, F., L. Chen, H. N. Zheng, and S. Wang (2007b), A parametric ray tracing study of superluminous auroral kilometric radiation wave modes, *J. Geophys. Res.*, *112*, A10214, doi:10.1029/2006JA012178.

Xiao, F., L. Chen, and J. Li (2008a), Energetic particles modeled by a generalized relativistic kappa-type distribution function in plasmas, *Plasma Phys. Controlled Fusion*, *50*, 105002, doi:10.1088/0741-3335/50/10/105002.

Xiao, F., L. Chen, H. Zheng, and S. Wang (2008b), A three-dimensional ray-tracing study of R-X mode waves during high geomagnetic activity, *Chin. Phys. Lett.*, *25*, 340–343, doi:10.1088/0256-307X/25/1/091.

Xue, S., R. Thome, and D. Summers (1996a), Growth and damping of oblique electromagnetic ion cyclotron waves in the Earth's magnetosphere, *J. Geophys. Res.*, *101*, 15,457–15,466.

Xue, S., R. Thome, and D. Summers (1996b), Parametric study of electromagnetic ion cyclotron instability in the Earth's magnetosphere, *J. Geophys. Res.*, *101*, 15,467–15,474.

Zhou, Q. H., Y. H. He, Z. G. He, and C. Yang (2010), Propagation characteristics of whistler-mode chorus during geomagnetic activities, *Chin. Phys. Lett.*, *27*, 055204, doi:10.1088/0256-307X/27/5/055204.